RSC Advances

ROYAL SOCIETY OF CHEMISTRY

www.rsc.org/advances

Targeting delivery and deep penetration using multistage nanoparticles for triple-negative breast cancer

Shaobo Ruan[a], Li Zhang[a], Jiantao Chen[a], Tingwei Cao[a], Yuting Yang[a], Yayuan Liu[a], Qin He[a], Fabao Gao[b,*] and Huile Gao[a,*]

[a]Key Laboratory of Drug Targeting and Drug Delivery Systems, West China School of Pharmacy, Sichuan University, No. 17, Block 3, Southern Renmin Road, Chengdu 610041, China
[b]Molecular Imaging Center, Department of Radiology, West China Hospital, Sichuan University, No. 37 Guo Xue Xiang, Chengdu, Sichuan 610041, China
*Corresponding Authors: Fax/Tel: 86 28 85502532. E-mail: gaohuile@scu.edu.cn. E-mail: gaofabao@yahoo.com.

ABSTRACT: Targeting delivery and deep penetration have been attracting tremendous attention in triple-negative breast cancer (TNBC) theranostics. Herein, we reported a novel multistage system (G-AuNPs-DOX-RRGD) with active targeting effect and size-changeable property to inhibit tumor growth and metastasis in 4T1 xenograft bearing mice. The system was constructed through fabricating small-size gold nanoparticles (AuNPs) onto matrix metalloproteinase-2 (MMP-2) degradable gelatin nanoparticles (GNPs). Doxorubicin (DOX) was tethered onto AuNPs via a pH sensitive hydrazone bond, and RRGD, a tandem peptide of RGD and octarginine, was surface-decorated onto the system to improve its tumor targeting efficiency. In vitro, the G-AuNPs-DOX-RRGD could shrink from 185.9 nm to 71.2 nm after 24 h incubation with MMP-2 and the DOX was released in a pH-dependent manner. Tumor spheroid penetration and collagen diffusion demonstrated G-AuNPs-DOX-RRGD possessed best penetrating efficiency. In vivo, the G-AuNPs-DOX-RRGD actively targeted to 4T1 tumor and then penetrated through the interstitial matrix, resulting in enhanced accumulation in deep tumor region. Therefore, the G-AuNPs-DOX-RRGD could approach excellent anti-tumor capacity owing to the synergistic effect of RRGD and size-changeable property.

Keywords: targeting delivery, deep penetration, size-changeable, pH sensitive, MMP-2

Introduction

Triple-negative breast cancer (TNBC) is the most aggressive type of breast cancer, defined as tumors lacking estrogen receptor (ER), progesterone receptor (PR) and HER2/neu,[1,2] which represents high-grade tumors that are malignant and generally associated with regional node metastasis, and recur at distant tissue site.[3,4] Despite the efforts devoted in tumor diagnosis and treatment have prolonged the survival of breast cancer patients, while the TNBC is still to be leading cause of disproportionate morbidity and mortality.[5] The absence of most specific targeted therapeutics, dense tumor extracellular matrix (ECM) and elevated tumor interstitial fluid pressure (IFP) restricts the TNBC therapy. As a result, nanocarrier-based therapeutics calls for targeting delivery and efficient deep penetration in response to the challenges of TNBC therapies, such as short blood half-life, poor tumor targeting, insufficient tumor cell internalization and interstitial penetration.[6,7]

Systemic delivery of drug-loaded nanocarriers to tumor site within the blood-borne circulation is through the enhanced permeability and retention (EPR) effect, while the restricted by the poor targeting efficiency.[8-11] To improve this performance, nanocarriers are generally engineered with functional moieties that could actively recognize tumor related specific receptors and/or mediate cellular internalization. RGD can specifically target to $\alpha_v\beta_3$ receptors, which is involved in both TNBC cells and (tumor-induced) neovessels, leading to a high targeting efficiency.[12-14] However, RGD mediated transport possessed poor penetration efficiency, leading to a modest transcytosis of TNBC cells and neovessels.[15] Therefore, a tandem peptide RRGD, developed through direct conjugation of RGD peptide with octarginine, was employed to enhance cellular internalization and transcytosis of nanocarriers accompanying targeting effect.[16-18] Octarginine is a cell penetrating peptide that could improve the permeability of nanocarriers.[19] In combination, RRGD may significantly improve the tumor targeting and penetrating efficiency of nanocarriers in the delivery process to deep TNBC cells.

Penetration of nanotherapeutic to deep tumor region is restricted by the heterogeneity of tumor microenvironment posed by tumor ECM and elevated tumor IFP.[8,20] Therefore, delivery strategies to enhance deep penetrating efficiency have been focused on decreasing interstitial hypertension, normalizing interstitial matrix, stimulus-sensitive transport and tumor penetrating peptide.[21-24] The effectiveness of these approaches depends on pharmacology of the drug and biology of the tumor. While certain tumors may exhibit pronounced EPR effect, others do not such as 4T1 tumor, which has an ECM rich in collagen and fibronectin.[25,26] This TNBC type presents a biological barrier to delivery, contributing to a paradoxical requirement of permeability and retention because high tumor permeability requires small particle size while high tumor retention requires large particle size.[27-29] Thus, stimulus-sensitive size-changeable nanocarriers have been engaged and designed for drug delivery. This size change can be triggered by proteases that are overexpressed in tumor microenvironment, such as MMP-2.[30,31] Gelatin, the substrate of MMP-2, has been designed and showed stimulus responsiveness when used for constructing MMP-2 sensitive size-changeable delivery system.[8,32,33] Additionally, small-size gold

nanoparticles (AuNPs) have been proved with an excellent penetrating capacity through the vasculatures and tumor matrix.[34-36] Thus, we have proposed a size-changeable nanocarrier system (G-AuNPs) that conjugated small-size AuNPs with GNPs to form system with good retention because of the large size. After degradation by MMP-2, the G-AuNPs are shrunk to release AuNPs, which can further penetrate and accumulate in deep tumor regions.

pH sensitive release of drugs is also an important direction, which can mediate the release in specific lesion location. Hydrazone is a specific linker for acid sensitive release of drugs because it could hydrolyze and cleave in the low pH condition.[37-39] Generally, the normal physiological environment is neutral, while the pH of tumor microenvironment is as low as 6.0.[40,41] Thus hydrazone linker can be used for pH sensitive drug release in tumor because of the acidic microenvironment. Doxorubicin (DOX), one of the most common used chemotherapeutics, is combined with nanocarriers via hydrazone linker, enabling DOX loaded nanocarriers pH sensitive drug release capacity.

In this study, we proposed a nanocarriers-based drug delivery system with targeting capacity and size-changeable property to inhibit tumor growth and metastasis. The system, G-AuNPs-DOX-RRGD, which was fabricated with the degradable gelatin nanoparticle (GNPs), DOX tethered gold nanoparticles (AuNPs) and RRGD. Our previous research had validated the effectiveness of this size-changeable drug delivery system, while the poor targeting efficiency restricted its application.[42,43] Herein, G-AuNPs-DOX-RRGD possessed an excellent anti-tumor effect via a “two-step” delivery strategy. Firstly, the G-AuNPs-DOX-RRGD could actively target to 4T1 tumor (a breast cancer) through the mediation of RRGD. Secondly, after retained in tumor, the G-AuNPs-DOX-RRGD of large size could be shrunk to small-size AuNPs-DOX-RRGD, owing to the degradation of GNPs by the MMP-2. The AuNPs-DOX-RRGD could further penetrate through vasculature and interstitial matrix to deep tumor regions and then release DOX, resulting in an enhanced anti-tumor effect.

Materials and methods

Materials.

Chloroauric acid was purchased from Sinopharm Chemical Reagent Co. Ltd (Shanghai, China). Gelatin type A was purchased from MP Biomedicals (Santa Ana, USA). Doxorubicin Hydrochloride was obtained from Beijing Huafeng United Technology Co., Ltd (Beijing, China). Carboxyl-polyethylene glycol-thiol (CM-PEG-SH, MW=5000) and Thiol-polyethylene glycol (PEG-SH, MW=5000) were obtained from Laysan Bio Inc (Arab, AL, USA). Rat tail collagen I (C3867-1VL) was purchased from SIGMA-ALDRICH Corporation (USA). LysoTracker Red was gained from Life Technologies (Grand Island, NY, USA). R8-RGD was custom-synthesized by Sangon Biotech Co., Ltd (shanghai, China). 1-[3-(Dimethylamino)propyl]-3-ethylcarbodiimide Hydrochloride(EDC) and N-hydroxy-succinimide (NHS) were obtained from Keddia Reagent (Chengdu, China). Plastic cell culture dishes and plates were purchased from Wuxi NEST

Biotechnology Co Ltd (Wuxi, China). Rabbit anti-CD34 antibody was purchased from Abcam (Hong Kong) Ltd. (Hong Kong, China). Cy3-conjugated donkey anti-rabbit secondary antibody was purchased from Jackson ImmunoResearch Laboratories, Inc (West Grove, PA, USA). 4T1 cells were obtained from Chinese Academy of Sciences Cells Bank (Shanghai, China).

Female BALB/c mice (18 ± 2 g) were purchased from Dashuo Bio technology Co., Ltd, (Chengdu, China) and maintained under standard housing conditions. All animal experiments were carried out in accordance with guidelines evaluated and approved by the ethics committee of Sichuan University.

Synthesis of SH-R-Hyz-DOX and NH_2-Hyz-DOX

Thiol-alkyl-hydrazone bond-DOX (SH-R-Hyz-DOX) was synthesized according to a procedure elucidated in previous research.[17,34] Amino-hydrazone bond DOX (NH_2-Hyz-DOX) was synthesized using one-step pathway. In detail, 19.7 mg doxorubicin hydrochloride (0.0339 mmol, 1 eq) was dissolved in 5 mL anhydrous methanol and then added with 1.67 μL hydrazine hydrate (0.0339 mmol, 1.1 eq). The mixture was reacted in dark for 3 days at room temperature.

Preparation of G-AuNPs-DOX-RRGD

Citrate-stabilized AuNPs were prepared using a procedure according to our previous literature.[34] GNPs were prepared under the developed procedures of the two-step coagulation described in our previous research.[17] 6 mL of AuNPs solution were surface coated with SH-R-Hyz-DOX (60 μg) via the thiol-gold interaction to obtain the DOX-AuNPs. The prepared AuNPs-DOX was incubated with SH-PEG-COOH (18 μg), followed by 0.1 mL of EDC solution (26 mM) and NHS solution (43 mM). Then, the solution was centrifugalized to remove the unconjugated DOX and free EDC/NHS. The precipitate (AuNPs-DOX-PEG-NHS) was resuspended in 1 mL GNPs solution (20 mg/mL, pH 8.0) with a weight ratio of 3:100 (AuNPs: GNPs). The mixture was incubated at 150 rpm and under 37 ℃ for 8 h to obtain G-AuNPs-DOX-PEG solution. Finally, 30 μL of 1 mg/mL SH-PEG-RRGD was added to the solution to obtain G-AuNPs-DOX-RRGD.

Characterization of formulations

Particle size and zeta potential were determined by dynamic light scanning (DLS) analysis using a Malvern zetasizer nano ZS (Malvern, UK). The morphology of G-AuNPs-RRGD (with/without MMP-2), GNPs-RRGD and AuNPs-RRGD were captured by transmission electron microscope (TEM) (JEM-100CX, JEOL, Japan) after dyed by uranyl acetate, UV-Vis spectrum was performed on a cary 100 conc UV-Vis spectrophotometer (Varian、USA).

The in vitro release of DOX from different nanoparticles was evaluated using a Shimadzu RF-5301PC spectrofluorophotometer (RF-5301PC, Shimadzu, Japan). G-AuNPs-DOX-RRGD and GNPs-DOX-RRGD was resuspended in PBS at different pH (7.4, 6.8, 6.0 and 5.0) and deionized water respectively, free doxorubicin dispersed

in PBS (pH 7.4) was set as the control and the final concentration of DOX was 2.5 μM. The fluorescent emission spectra of G-AuNPs-DOX-RRGD in different pH situation were performed at different time intervals from 0 h to 48 h. All the procedures, including incubation and fluorescent detection, were performed at 37 ℃ in the dark.

Cellular uptake and subcellular localization

C6 cells were seeded onto glass coverslips that were placed in 6-well plates with 5×10^4/mL per well and allowed to grow until 60% confluent. After washed by PBS for twice, cells were treated with corresponding formulations for different time intervals. 30 minutes before the incubation ended, LysoTracker Red DND-99 (100 nmol/mL) was introduced into each well. After incubation, the cells were washed with PBS for twice and then fixed with 4% fresh paraformaldehyde for 30 min. The nuclei were further stained with 0.5 μg/mL of DAPI, images were captured using a confocal microscope ((LSM710, Carl Zeiss, Germany).

Tumor spheroid penetration

To prepare the three-dimensional tumor spheroids, 4T1 cells were seeded at a density of 5×10^3 cells/100 μL per well in 96-well plates pre-coated with 100 μL of 2% low-melting-temperature agarose. 48 h after the cells were seeded, tumor spheroids were formed and treated with free DOX, AuNPs-DOX-RRGD, GNPs-DOX-RRGD (pre-treatment with/without 300 ng MMP-2), G-AuNPs-DOX-PEG and G-AuNPs-DOX-RRGD (pre-treatment with/without 300 ng MMP-2) at an equivalent concentration of DOX (10 μg/mL). After 12 h of incubation, the spheroids were rinsed with ice-cold PBS for three times and fixed with 4% paraformaldehyde for 12 h. Then the spheroids were transferred to glass bottom petri-dish and covered by glycerophosphate. Fluorescent intensity was observed by a confocal microscope (LSM710, Carl Zeiss, Germany).

Collagen gel diffusion

Collagen hydrogels were prepared by mixing the following components in order on ice: 141.75 μL of 4.5 mg/mL rat tail collagen I, 3.8 μL of 1 M sodium hydroxide, and 19.5 μL of 0.17 M EDTA. The final concentration of collagen was 3.86 mg/mL and EDTA was 20 mM. After vortexing, the gel was added to partially fill a microslide capillary tube (emsdiasum, USA), then incubated overnight at 37 ℃. The G-AuNPs-DOX-RRGD was incubated with 300 ng of activated MMP-2 for 12 h in 50 mM Hepes and 2 mM $CaCl_2$. At the end of 12 h, EDTA was added to give a final concentration of 20 mM. 20 μL of G-AuNPs-DOX-RRGD solution before or after incubation with MMP-2 was added into the capillary tube and placed in contact with the surface of the collagen gel. The G-AuNPs-DOX-PEG, GNPs-DOX-RRGD, AuNPs-DOX-RRGD and free DOX were also prepared as described above. The concentrations of these formulations were adjusted to equivalent so that they gave the same signal intensity. The images were captured using a confocal microscope (LSM710, Carl Zeiss, Germany).

In vivo tumor and tissue distribution

4T1 tumor bearing BALB/c mice were established as described previously.[44] Female BALB/c mice were anesthetized and then 0.1 mL of PBS containing 1×10^6 4T1 cells was slowly injected into the left upper thigh subcutaneous region. Two weeks later, the subcutaneous 4T1 tumor bearing mice were randomly divided in 5 groups (3 mice/group): DOX solution, G-AuNPs-DOX-RRGD, G-AuNPs-DOX-PEG, GNPs-DOX-RRGD and AuNPs-DOX-RRGD. Each mouse was i.v. administrated with corresponding formulations at an equivalent DOX of 3 mg/kg through tail vein. At 24 h after injection, three mice from each group were sacrificed and purfused with PBS followed by 4% paraformaldehyde. Then the tissues were sampled and fixed with 4% paraformaldehyde, tissues were further dehydrated using 15% sucrose followed with 30% sucrose. Consecutive frozen sections of 10 μm thicknesses were prepared. Tumor slices were stained with rabbit anti-CD34 antibody and Cy3-labled donkey anti-rabbit secondary antibody with a procedure established previously.[45] Slices of other tissues were directly stained with 0.5 μg/mL of DAPI. Then the fluorescent distribution was captured by a confocal microscope (LSM710, Carl Zeiss, Germany).

Anti-tumor effect

4T1 tumor bearing mice were established as described above. Ten days after implantation, the mice were randomly divided into 5 groups (7 mice per group): saline group, free DOX group, AuNPs-DOX-RRGD group, GNPs-DOX-RRGD group, G-AuNPs-DOX-PEG group and G-AuNPs-DOX-RRGD. Each mouse received a dose of 3 mg/kg doxorubicin every 2 days for 6 times. The tumor volume and body weight were determined before every injection. One day after the last injection, all the mice were sacrificed and the organs were extracted and fixed with 4% paraformaldehyde. Then the hearts, lungs and tumors were sampled and applied for hematoxylin and eosin (HE) staining.

Statistical analysis

Statistical differences were evaluated with Student's test and performed by one-way ANOVA for multiple groups, and p value<0.05, <0.01 and <0.005 were considered indications of statistical difference and statistically significant difference, respectively.

Results and Discussion

Characterization of size shrinking

The yield of SH-R-Hyz-DOX and NH_2-Hyz-DOX was 31.6% and 91.2% respectively. The initial hydrated diameter of AuNPs and GNPs was 21.2 nm and 143.7 nm (Table 1 and Fig. S1), the particle size of AuNPs-DOX-RRGD and GNPs-DOX-RRGD was 36.2 and 150.2 respectively. After conjugation of GNPs with AuNPs-DOX and NH_2-PEG-R8-RGD, the size of G-AuNPs-DOX-RRGD increased to 185.9 nm, indicating G-AuNPs-DOX-RRGD has been successfully fabricated.

Table 1. Physicochemical characterization of different formulations (data represent mean data ± SD, n=3).

Formulations	Particle size (nm)	PDI	Zeta Potential (mV)
AuNPs	21.3±0.37	0.227	-17.69±0.32
GNPs	140.1±1.06	0.146	-9.13±0.16
AuNPs-DOX-RRGD	36.2±1.26	0.278	-13.47±0.19
GNPs-DOX-RRGD	150.2±1.67	0.230	-6.71±0.10
G-AuNPs-DOX-PEG	180.3±0.75	0.261	-10.3±0.14
G-AuNPs-DOX-RRGD	185.9±1.02	0.285	-8.87±0.11

Fig. 1 Characterization of different particles. A: Particle size and zeta potential of G-AuNPs-DOX-RRGD, GNPs-DOX-RRGD and AuNPs-DOX-RRGD after incubation with MMP-2 (300 ng/mL) at different time intervals. B: DLS data of G-AuNPs-DOX-RRGD. C: TEM image of G-AuNPs-DOX-RRGD. D: DLS data of G-AuNPs-DOX-RRGD after 24 h incubation with MMP-2. E: TEM image of G-AuNPs-DOX-RRGD after 24 h incubation with MMP-2. F: TEM image of AuNPs. G: TEM image of GNPs. H: UV-Vis spectra of AuNPs, GNPs and G-AuNPs, inner picture display the photo image. I: MTT assays of AuNPs, GNPs and G-AuNPs after incubation with 4T1 cells for 48 h.

To evaluate the changeable capacity of G-AuNPs-DOX-RRGD, the particle sizes of G-AuNPs-DOX-RRGD, GNPs-DOX-RRGD and AuNPs-DOX-RRGD were recorded after incubation with MMP-2 for 0, 1, 2, 4, 12 and 24 h. With the expanding of incubated time, the particle sizes of G-AuNPs-DOX-RRGD and GNPs-DOX-RRGD were decreased gradually (Fig. 1A). After 24 h incubation, the G-AuNPs-DOX-RRGD and GNPs-DOX-RRGD shrunk from 185.9 nm and 150.2 nm respectively to 71.2 nm and 56.9 nm respectively, suggesting the G-AuNPs-DOX-RRGD and GNPs-DOX-RRGD could be shrunk by MMP-2. The results were consistent with the DLS distribution and TEM images (Fig. 1B, C, D and E). While the AuNPs-DOX-RRGD did not show obvious changes even at the end of incubation, indicating the AuNPs could not be degraded by MMP-2. Additionally, TEM images of AuNPs and GNPs were displayed as control (Fig. 1F and G), and the zeta potential of these particles had no obvious change during incubation with MMP-2. All these results indicated the shrink of G-AuNPs-DOX-RRGD was caused by the degradation of GNPs, which was the substrate of the MMP-2.[8]

Then the optical property of these three basic nanocarriers was characterized using UV-Vis spectrophotometer. The UV-Vis spectra of AuNPs, GNPs and G-AuNPs displayed different characteristic absorption (Fig. 1H). The characteristic absorption peak of AuNPs was 482 nm in visible light region, while characteristic peaks of GNPs were 264 nm and 228 nm in UV light region. After combination with AuNPs and GNPs, the spectral of G-AuNPs showed mutual characteristic peaks, which was close to the corresponding peaks of AuNPs and GNPs respectively, indicating the G-AuNPs system was successfully conjugated. We also evaluated the cytotoxicity of these three nanocarriers (Fig. 1I), after 24 h incubation with G-AuNPs, GNPs and AuNPs, the viability of 4T1 cells was still as high as 84.1%, 86.2% and 88.3% even at each

highest incubated concentration, suggesting these nanocarriers were low cytotoxicity.[33,46]

In vitro release of doxorubicin

The fluorescence of doxorubicin was quenched when it was anchored onto nanoparticles because of the nanosurface energy transfer (NSET) effect.[40] To evaluate the release behavior of DOX from these particles, we chosen G-AuNPs-DOX-RRGD and GNPs-DOX-RRGD to determine the hydrolytic degree of the two different pH sensitive DOX probe at different pH values using fluorescence scanning. At the beginning of incubation, the fluorescence of G-AuNPs-DOX-RRGD was almost quenched in all pH conditions (Fig. 2A), and the fluorescence of GNPs-DOX-RRGD was also significantly quenched (Fig. 2B), illustrating the fluorescence of DOX could be quenched by AuNPs and GNPs when conjugated onto them. After 4 h incubation, the fluorescence of both particles was recovered gradually (Fig. 2C and D). The fluorescent intensity of releasing DOX from G-AuNPs-DOX-RRGD and GNPs-DOX-RRGD in pH 5.0 was much higher than that of pH 6.0, 6.8, 7.4 and deionized water, indicating the low pH value could facilitate the hydrolysis of hydrazone bond and thus released DOX.[47,48] Further expanding the incubation time could lead to significant recovery of fluorescent intensity (Fig. 3E and F, Fig. S2), suggesting the hydrolysis of hydrazone was in a time-dependent manner.[34] The cumulative releasing ratio of DOX from G-AuNPs-DOX-RRGD and GNPs-DOX-RRGD were as high as 96.09% and 86.67% respectively after 48 h incubation in pH 5.0, suggesting the releasing of both pH sensitive DOX probe was effective. All these results elucidated the validity of pH sensitivity of both DOX fluorescent probes, demonstrating these particles could be response to the acidic condition of tumor microenvironment.

Fig. 2 Characterization of releasing DOX. A: Fluorescent emission spectra of releasing DOX from G-AuNPs-DOX-RRGD at 0 h under different pH condition. B: Fluorescence emission spectra of releasing DOX from GNPs-DOX-RRGD at 0 h under different time pH conditions. C: Fluorescent emission spectra of releasing DOX from G-AuNPs-DOX-RRGD at 4 h under different pH condition. D: Fluorescence emission spectra of releasing DOX from GNPs-DOX-RRGD at 4 h under different time pH conditions. E: Fluorescence emission spectra of releasing DOX from G-AuNPs-DOX-RRGD under pH 5.0 at different time from 0 to 48 h. F: Fluorescence emission spectra of releasing DOX from GNPs-DOX-RRGD under pH 5.0 at different time from 0 to 48 h.

Cellular uptake and subcellular localization

To determine internalized behavior of these particles by 4T1 cells, in vitro cellular uptake was qualitatively and quantitatively evaluated. In microscope images, the fluorescence of releasing DOX was successfully observed in all groups (Fig. 3A). These images showed that particles could be internalized into cells in a time-dependent manner and release DOX. The uptake intensity of RRGD decorated particles was much higher than that of G-AuNPs-DOX-PEG, suggesting the RRGD could enhance the internalization of particles. The results were also validated by

quantitative data (Fig. S3). After labeled with endosomes, the releasing DOX from G-AuNPs-DOX-RRGD showed well colocalization with endosomes after 15 min and 1 h incubation (Fig. 3B), illustrating the endosomes were involved in the internalization procedure.[16,38] Increasing the incubating time to 4 h and 24 h decreased the colocalization, leading to more DOX enter into cytoplasm and nuclei, probably owing to the escape of G-AuNPs-DOX-RRGD from endosomes, which was consistent with other study [49]. The internalized and released behavior of other particles was in a similar manner (Fig. S4). The results were benefit for DOX induced apoptosis and consistent with previous research.[34]

Fig. 3 Cellular uptake and subcellular localization. A: 4T1 cell uptake of G-AuNPs-DOX-RRGD, G-AuNPs-DOX-PEG, GNPs-DOX-RRGD, AuNPs-DOX-RRGD and free DOX after 0.25 h, 1 h, 4 h and 24 h incubation, green represents DOX and bar represents 50 μm. B: 4T1 cell subcellular localization of G-AuNPs-DOX-RRGD with endosomes, green represents DOX, red represents endosomes and bar represents 20μm.

Tumor spheroids penetration

Monolayer cellular uptake could only show internalizing efficiency, but it may not accurately reflect the penetrating effect in solid tumor because of the difference between cell monolayer and solid tumor.[50] In vitro tumor spheroid could imitate the in vivo status of tumor because the tumor spheroids are characterized with poor drug penetration, altered enzyme activity and viable rim with gradients of oxygen tension, etc.[51,52] Thus, the 4T1 tumor spheroids were chosen to evaluate the penetrating efficiency of these particles. The distribution of G-AuNPs-DOX-RRGD in all sections of spheroid was observed and the images showed the releasing DOX was mainly located in edge regions rather than in central region (Fig. 4A), suggesting the G-AuNPs-DOX-RRGD was difficult to diffuse into the deep regions due to its large size. After 12 h pre-incubation with MMP-2, the size of G-AuNPs-DOX-RRGD was shrunk to small, resulting in more particles penetrated into deep regions and then released DOX. Similar penetrating results were observed in the distribution of GNPs-DOX-RRGD (with/without MMP-2). Comparatively, the distribution of AuNPs-DOX-RRGD displayed stronger intensity than that of G-AuNPs-DOX-RRGD in the deep section of tumor spheroid, which further indicated the small particle size possessed an advantage in penetrating into deep regions of tumor spheroid. Additionally, the distribution of G-AuNPs-DOX-PEG was much lower than that of G-AuNPs-DOX-RRGD, indicating the RRGD also acted as a primary role in penetrating through tumor spheroid, which was consistent with previous studies.[53,54]

Fig. 4 Tumor spheroids penetration. A: Fluorescence distribution of G-AuNPs-DOX-RRGD (with/without MMP-2), G-AuNPs-DOX-PEG and AuNPs-DOX-RRGD in 4T1 tumor spheroids after 12 h incubation, the concentration of DOX was in an equivalent dose of 10 μg/mL, bar represents 200 μm. B: Semi-quantitative intensity of these particles at central sections of tumor

spheroids. C: Semi-quantitative intensity of these particles at central sections of tumor spheroids. D: Penetrating percentage of these particles at 20 and 140 μm distance from the bottom, *p<0.05.

Semi-quantitative intensity in the central and edge regions of tumor spheroids was both measured to evaluate the distribution of these particles (Fig. 4B and C). The intensity decreased with the extension of distance from tumor spheroid bottom, which was consistent with qualitative results. Furthermore, the penetrating percentage (fluorescent intensity of central region/edge region) was introduced to evaluate the penetrating efficiency of different particles (Fig. 4D). The penetrating percentage of different particles at 20 μm distance from the bottom of tumor spheroids was similar. However, at 140 μm, the penetrating percentage of G-AuNPs-DOX-RRGD after pre-treatment with MMP-2 was considerably higher than that of G-AuNPs-DOX-RRGD without pre-treatment, suggesting the size-shrink could enhance the penetrating efficiency.[8] All the qualitative and quantitative results demonstrated that size-shrinking property was benefit for penetrating through tumor spheroids.

Collagen diffusion

To further investigate the capacity of MMP-2 to shrink the size of G-AuNPs-DOX-RRGD in vitro, the distribution in the collagen gel was observed using fluorescent detection after 12 h incubation (Fig. 5). In the distance 1000-2000 μm from the initial position, the fluorescence distribution of these particles displayed no significant difference, suggesting these DOX tethered particles could diffuse into the collagen gel to a certain degree of distance. With the extension of distance (6000-7000 μm from the initial position), the distribution of G-AuNPs-DOX-RRGD was obviously decreased, after 24 h pre-incubation with MMP-2, the distribution was significantly improved, indicating MMP-2 could shrink the G-AuNPs-DOX-RRGD and thus enhanced the diffusion through collagen gel. The distribution of GNPs-DOX-RRGD was close to that of G-AuNPs-DOX-RRGD, suggesting that the triggering of size-shrink was due to the degradation of GNPs. AuNPs-DOX-RRGD could efficiently diffuse through the collagen gel because of its small size. However, there is no obvious difference in the distribution of G-AuNPs-DOX-RRGD and G-AuNPs-DOX-PEG, demonstrating that RRGD could not enhance the diffusion in collagen gel due to the non-receptor mediated delivery. The results further verified that the size-shrink could play an important role in improving penetrating efficiency, which was consistent with tumor spheroids results.

Fig. 5 Collagen diffusion of G-AuNPs-DOX-RRGD (with/without MMP-2), G-AuNPs-DOX-PEG, GNPs-DOX-RRGD (with/without MMP-2), AuNPs-DOX-RRGD and free DOX, green represents DOX and bar represents 200 μm.

Ex vivo imaging

4T1 tumor xenografts bearing mice were used to evaluate the in vivo targeting and penetrating efficiency of the G-AuNPs-DOX-RRGD. The ex vivo imaging displayed highest intensity of G-AuNPs-DOX-RRGD in 4T1 tumor using epi-fluorescent

detection (Fig. 6A), suggesting G-AuNPs-DOX-RRGD could target to tumor site. The semi-quantitative signal reflected directly that the G-AuNPs-DOX-RRGD had a highest accumulation in tumor (Fig. 6B). Here, the tumor/liver (T/L) ratio was introduced to evaluate the targeting efficiency of these particles, the T/L ratio of G-AuNPs-DOX-PEG was 0.81, owing to the EPR effect. While the T/L ratio of G-AuNPs-DOX-RRGD, GNPs-DOX-RRGD and AuNPs-DOX-RRGD was as high as 1.58, 1.13 and 1.31 respectively, suggesting RRGD could significantly improve tumor targeting efficiency.[16,55] Ex vivo imaging and semi-quantitative data of other tissues showed that particles were mainly accumulated in kidney (Fig. 6C and D), indicating kidney was the main metabolic organs.

Fig. 6 Ex vivo imaging of 4T1 tumor. A: Ex vivo imaging of 4T1 tumor after 24 h incubation with G-AuNPs-DOX-RRGD, G-AuNPs-DOX-PEG, GNPs-DOX-RRGD, AuNPs-DOX-RRGD and Free DOX. B: Semi-quantitative signal of tumors after 24 h incubation with different particles. C: Ex vivo imaging of normal tissues. D: Semi-quantitative signal of normal tissues. E: Distribution of releasing DOX in outer and inner tumor. F: Penetrating efficiency of different particles, *$p<0.05$.

To directly investigate the penetrating efficiency of G-AuNPs-DOX-RRGD, the DOX concentrations in the inner part and outer part of tumor were quantitatively determined using LC/MS-MS (Fig. 6E). The concentration of DOX in the outer part of tumor treated with G-AuNPs-DOX-RRGD was similar to GNPs-DOX-RRGD and AuNPs-DOX-RRGD while higher than G-AuNPs-DOX-PEG and free DOX, contributing to the targeting effect of RRGD. Due to the high interstitial hypertension and less neovessels in the inner part of tumor, the concentration of DOX was lower than that in the outer tumor. Thus, the penetration percentage (inner tumor/outer tumor) was introduced (Fig. 6F) to determine the penetrating efficiency, the penetration percentages of G-AuNPs-DOX-RRGD, G-AuNPs-DOX-PEG, GNPs-DOX-RRGD, AuNPs-DOX-RRGD and Free DOX were 75.5%, 32.1%, 57.5%, 60.5% and 24.1% respectively, suggesting G-AuNPs-DOX-RRGD possessed significant advantage in penetrating through the solid tumor. The AuNPs-DOX-RRGD with small size was featured with better transvascular and interstitial transport effect,[27,28,56] while it may has a relatively short blood half-life and distribute to normal tissue. In contrast, G-AuNPs-DOX-RRGD with large size could reach long circulation owing to its relatively longer blood half-life.[57,58] Therefore, systemic injection with large-size G-AuNPs-DOX-RRGD could reach an initial higher accumulation and extravasation in tumor site accompanying the mediation of RRGD. After transporting the tumor vessel wall into the tumor interstitial matrix, the G-AuNPs-DOX-RRGD could be degraded by the overexpressed MMP-2 and turned to be small-size AuNPs-DOX-RRGD, which could further achieve enhanced penetration through interstitium to deep tumor region, resulting in the highest accumulation of G-AuNPs-DOX-RRGD in deep tumor region. All these results demonstrated the validity of this strategy in vivo.

Tumor distribution

After neovessels were stained with anti-CD34 antibody, the fluorescent distribution in tumor slices demonstrated G-AuNPs-DOX-RRGD had a good accumulation and colocalization in tumor edge region, as well as the GNPs-DOX-RRGD and AuNPs-DOX-RRGD (Fig. 7A), while the distribution of G-AuNPs-DOX-PEG was much lower than that of G-AuNPs-DOX-RRGD, GNPs-DOX-RRGD and AuNPs-DOX-RRGD, which was due to the targeting effect of RRGD.[59] The distribution of AuNPs-DOX-RRGD was relatively weaker than that of G-AuNPs-DOX-RRGD, which was possibly due to their poor tumor distribution and extravasation of small-size AuNPs-DOX-RRGD in the circulation. In the deep region of 4T1 tumor (3 mm apart from the edge), the distribution of G-AuNPs-DOX-RRGD was obviously away from the localization of neovessels (Fig. 7B), indicating the G-AuNPs-DOX-RRGD could efficiently penetrate through vasculatures and retained in deep tumor regions even with the existence of high interstitial hypertension. However, the GNPs-DOX-RRGD displayed weaker distribution than that of G-AuNPs-DOX-RRGD in the deep region, possibly owing to the distinguishing pH sensitivity of DOX probe,[48] which in turn lead to a deferred DOX release of GNPs-DOX-RRGD. Besides, the distribution of these particles in normal tissue slices displayed no significant difference (Fig. S5), which was consistent with the ex vivo imaging results. In combination with in vitro and in vivo experiments, the results demonstrated the RRGD decoration could improve tumor targeting efficiency and MMP-2 triggering size-change could further enhance the penetrating efficiency, making the G-AuNPs-DOX-RRGD to be efficient nanocarriers that meet the complex requirements existed in delivery process.

Fig. 7 Distribution of different particles in tumor slices. A: Distribution in edge region of tumor slices. B: Distribution in deep region of tumor slices, green represents DOX, red represents CD34 and bar represents 100 μm.

Anti-tumor effect

The viabilities of 4T1 cells after incubated with different particles were decreased apparently with the increasing concentration of DOX (Fig. 8A), suggesting all the formulations could induce the apoptosis of 4T1 cells. To evaluate in vivo anti-tumor effect of different formulations, the volumes of 4T1 tumor were determined (Fig. 8B), although free DOX could significantly induce apoptosis of 4T1 cells, while the tumor growth rate of 4T1 bearing mice treated with free DOX showed an uncontrollable trend, which was ascribed to the poor tumor targeting efficiency as demonstrated in the tumor distribution study. G-AuNPs-DOX-PEG could passively target to tumor site via EPR effect, leading to lower tumor growth rate, while the poor targeting efficiency of G-AuNPs-DOX-PEG restricted its anti-tumor effect. Comparably, the tumor growth rate of G-AuNPs-DOX-RRGD displayed a best inhibition compared with other groups. The photo images of stripping tumors also displayed best anti-tumor effect of G-AuNPs-DOX-RRGD (Fig. 8C and Fig. S6), which were consistent with the quantitative data. Three main reasons may contribute to the results: first, the G-AuNPs-DOX-RRGD could obtain relatively higher tumor distribution and

extravasation owing to its longer circulation. Second, RRGD could mediate the active delivery of G-AuNPs-DOX-RRGD to tumor, which further improved the targeting efficiency.[60] Third, after transporting cross vasculature walls, the MMP-2 sensitive size-changeable property could enhance the penetration of G-AuNPs-DOX-RRGD through interstitium into deep tumor region. All these reasons eventually lead to the highest accumulation in deep tumor region and best anti-tumor effect.

Fig. 8 Anti-tumor effects after treated with G-AuNPs-DOX-RRGD, G-AuNPs-DOX-PEG, GNPs-DOX-RRGD, AuNPs-DOX-RRGD and Free DOX and normal saline. A: MTT assay of 4T1 cells treated with different groups at a serious of concentrations. B: Average volumes of 4T1 tumor treated with different groups, *$p<0.05$, **$p<0.01$. C: Image of 4T1 tumor extracted from the mice at the end of experiment. D: HE staining of 4T1 tumor from mice treated with different groups, bar represents 100 μm.

HE staining of tumors was prepared to investigate the cell apoptosis (Fig. 8D). The tumor cells were clearly observed in free DOX and normal saline groups, which was consistent with tumor growth rate of these two groups. However, in G-AuNPs-DOX-RRGD group, the density of tumor cells was much lower than that of other groups, including the GNPs-DOX-RRGD and AuNPs-DOX-RRGD group, further indicating tumors treated with G-AuNPs-DOX-RRGD underwent more apoptosis than other groups because of its highest accumulation and pH triggering DOX release.

Here, owing to the high metastasis and invasion of the 4T1 tumor cells, the cells may metastasize to other normal tissues.[44] Meanwhile, the lung was vulnerable to the high metastatic tumor cells.[4,61] Photo images of stripping lungs directly reflect the pulmonary metastatic nodules of 4T1 tumor bearing mice (Fig. 9A), the pulmonary metastatic nodules could be obviously observed in lungs treatment with normal saline and free DOX. However, in G-AuNPs-DOX-RRGD treated mice, there were no significant pulmonary metastatic nodules, suggesting the G-AuNPs-DOX-RRGD could efficiently inhibit the metastasis of 4T1 tumor cells. The numbers of pulmonary metastatic nodules was calculated to further validate the anti-metastatic effect (Fig. 9B), in G-AuNPs-DOX-RRGD group, the numbers were least, indicating the G-AuNPs-DOX-RRGD possessed a best anti-metastasis effect, which was consistent with the images result. In addition, HE staining of lung was prepared to determine the anti-metastasis effect (Fig. 9C), in lungs treatment with normal saline, the metastatic tumor cells could be observed obviously. Area of metastatic tumor cells in G-AuNPs-DOX-PEG group was relatively smaller than that of free DOX and normal saline. However, in lungs treated with G-AuNPs-DOX-RRGD groups, no obvious metastatic regions were observed, suggesting G-AuNPs-DOX-RRGD also exhibit significant anti-metastatic effect to the pulmonary metastasis of 4T1 tumor cells, which was mainly because the G-AuNPs-DOX-RRGD could inhibit the growth of tumor cells and thus inhibit its metastasis, the potential mechanism of combined anti-metastasis effect was remained to discover.

Fig. 9 Anti-metastatic effect in 4T1 tumor models after treatment with G-AuNPs-DOX-RRGD, G-AuNPs-DOX-PEG, GNPs-DOX-RRGD, AuNPs-DOX-RRGD and Free DOX and normal saline. A: Photo images of pulmonary metastatic nodules after treated with different groups. B: Numbers of pulmonary metastatic nodules of every group, *p<0.05, **p<0.01. C: HE staining of lungs treated with different groups, arrow indicated metastatic region, arrow represents tumor regions and bar represents 200 μm.

Conclusion

We have developed a novel tumor microenvironment sensitive drug delivery system fabricated by the changeable GNPs, DOX tethered AuNPs and RRGD. The system, G-AuNPs-DOX-RRGD, possessed a capacity of targeting delivery to 4T1 cells and size-changeable property, resulting in an excellent anti-tumor effect to 4T1 bearing mice. The in vitro and in vivo experiments showed the RRGD decoration could significantly improve the tumor targeting efficiency and MMP-2 triggering size-changeable property was benefit for the subsequent penetration into deep tumor regions. Meanwhile, the release of DOX is a pH dependent manner because of the low pH in tumor microenvironment. In combination, G-AuNPs-DOX-RRGD showed a precise targeting efficiency and deep tumor penetration. It is envisioned that the validity of G-AuNPs-DOX-RRGD will provide opportunities to explore more functional drug delivery systems for targeting delivery and deep penetration of multiple tumors in the future.

Associated content

Supporting information

DLS data of different particles; Fluorescent emission spectra of GNPs-DOX-RRGD; Quantitative cellular uptake; Subcellular localization; Fluorescent distribution in tissue slices; Anti-tumor effect. This supporting information is available free of charge on the ACS Publications website at

Author information

Corresponding authors

*E-mail: qinhe@scu.edu.cn.
*E-mail: gaohuile@scu.edu.cn. Fax/Tel: 86 28 85502532

Notes

The authors declare no competing financial interest.

Acknowledgments:

This work was supported by the National Natural Science Foundation of China (81402866).

REFERENCES

1 S. Abdelhamed, S. Yokoyama, A. Refaat, K. Ogura, H. Yagita, S. Awale and I. Saiki, Piperine enhances the efficacy of TRAIL-based therapy for triple-negative breast cancer cells, *Anticancer Res*, 2014, 34, 1893-1899.

2 M. Singh, I. Ramos, D. Asafu-Adjei, W. Quispe-Tintaya, D. Chandra, A. Jahangir, X. Zang, B.B. Aggarwal and C. Gravekamp, Curcumin improves the therapeutic efficacy of Listeria(at)-Mage-b vaccine in correlation with improved T-cell responses in blood of a triple-negative breast cancer model 4T1, *Cancer Med*, 2013, 2, 571-582.
3 R. Dent, M. Trudeau, K.I. Pritchard, W.M. Hanna, H.K. Kahn, C.A. Sawka, L.A. Lickley, E. Rawlinson, P. Sun and S.A. Narod, Triple-negative breast cancer: clinical features and patterns of recurrence, *Clin Cancer Res*, 2007, 13, 4429-4434.
4 P. Xu, H. Yu, Z. Zhang, Q. Meng, H. Sun, X. Chen, Q. Yin and Y. Li, Hydrogen-bonded and reduction-responsive micelles loading atorvastatin for therapy of breast cancer metastasis, *Biomaterials*, 2014, 35, 7574-7587.
5 D. Spano, J.C. Marshall, N. Marino, D. De Martino, A. Romano, M.N. Scoppettuolo, A.M. Bello, V. Di Dato, L. Navas, G. De Vita, C. Medaglia, P.S. Steeg and M. Zollo, Dipyridamole prevents triple-negative breast-cancer progression, *Clin Exp Metastasis*, 2013, 30, 47-68.
6 D. Ling, W. Park, S.J. Park, Y. Lu, K.S. Kim, M.J. Hackett, B.H. Kim, H. Yim, Y.S. Jeon, K. Na and T. Hyeon, Multifunctional tumor pH-sensitive self-assembled nanoparticles for bimodal imaging and treatment of resistant heterogeneous tumors, *J Am Chem Soc*, 2014, 136, 5647-5655.
7 J. Peng, T. Qi, J. Liao, B. Chu, Q. Yang, Y. Qu, W. Li, H. Li, F. Luo and Z. Qian, Mesoporous magnetic gold "nanoclusters" as theranostic carrier for chemo-photothermal co-therapy of breast cancer, *Theranostics*, 2014, 4, 678-692.
8 C. Wong, T. Stylianopoulos, J.A. Cui, J. Martin, V.P. Chauhan, W. Jiang, Z. Popovic, R.K. Jain, M.G. Bawendi and D. Fukumura, Multistage nanoparticle delivery system for deep penetration into tumor tissue, *Proc Natl Acad Sci*, 2011, 108, 2426-2431.
9 H. Gao, J. Qian, S. Cao, Z. Yang, Z. Pang, S. Pan, L. Fan, Z. Xi, X. Jiang and Q. Zhang, Precise glioma targeting of and penetration by aptamer and peptide dual-functioned nanoparticles, *Biomaterials*, 2012, 33, 5115-5123.
10 H. Kobayashi, R. Watanabe and P.L. Choyke, Improving conventional enhanced permeability and retention (EPR) effects; what is the appropriate target?, *Theranostics*, 2013, 4, 81-89.
11 Y. Wen, S.L. Roudebush, G.A. Buckholtz, T.R. Goehring, N. Giannoukakis, E.S. Gawalt and W.S. Meng, Coassembly of amphiphilic peptide EAK16-II with histidinylated analogues and implications for functionalization of beta-sheet fibrils in vivo, *Biomaterials*, 2014, 35, 5196-5205.
12 L. Bello, M. Francolini, P. Marthyn, J. Zhang, R.S. Carroll, D.C. Nikas, J.F. Strasser, R. Villani, D.A. Cheresh and P.M. Black, Alpha(v)beta3 and alpha(v)beta5 integrin expression in glioma periphery, *Neurosurgery*, 2001, 49, 380-389; discussion 390.
13 A. Bunschoten, T. Buckle, N.L. Visser, J. Kuil, H. Yuan, L. Josephson, A.L. Vahrmeijer and F.W. van Leeuwen, Multimodal interventional molecular imaging of tumor margins and distant metastases by targeting alphavbeta3 integrin, *Chembiochem*, 2012, 13, 1039-1045.
14 K. Chen and X. Chen, Integrin targeted delivery of chemotherapeutics, *Theranostics*, 2011, 1, 189-200.
15 J.G. Parvani, M.D. Gujrati, M.A. Mack, W.P. Schiemann and Z.R. Lu, Silencing beta3 Integrin by Targeted ECO/siRNA Nanoparticles Inhibits EMT and Metastasis of Triple Negative Breast Cancer, *Cancer Res*, 2015,
16 Y. Liu, R. Ran, J. Chen, Q. Kuang, J. Tang, L. Mei, Q. Zhang, H. Gao, Z. Zhang and Q. He, Paclitaxel loaded liposomes decorated with a multifunctional tandem peptide for glioma targeting, *Biomaterials*, 2014, 35, 4835-4847.
17 S. Ruan, Q. He and H. Gao, Matrix metalloproteinase triggered size-shrinkable gelatin-gold fabricated nanoparticles for tumor microenvironment sensitive penetration and diagnosis of glioma, *Nanoscale*, 2015,
18 Y. Wen, W. Liu, C. Bagia, S. Zhang, M. Bai, J.M. Janjic, N. Giannoukakis, E.S. Gawalt and W.S. Meng, Antibody-functionalized peptidic membranes for

neutralization of allogeneic skin antigen-presenting cells, *Acta Biomater*, 2014, 10, 4759-4767.
19 H. Gao, Q. Zhang, Z. Yu and Q. He, Cell-penetrating peptide-based intelligent iposomal systems for enhanced drug delivery, *Curr Pharm Biotechnol*, 2014, 15, 210-219.
20 C.H. Heldin, K. Rubin, K. Pietras and A. Ostman, High interstitial fluid pressure - an obstacle in cancer therapy, *Nat Rev Cancer*, 2004, 4, 806-813.
21 T. Stylianopoulos and R.K. Jain, Combining two strategies to improve perfusion and drug delivery in solid tumors, *Proc Natl Acad Sci U S A*, 2013, 110, 18632-18637.
22 P.A. Netti, D.A. Berk, M.A. Swartz, A.J. Grodzinsky and R.K. Jain, Role of extracellular matrix assembly in interstitial transport in solid tumors, *Cancer Res*, 2000, 60, 2497-2503.
23 L. Zhu, T. Wang, F. Perche, A. Taigind and V.P. Torchilin, Enhanced anticancer activity of nanopreparation containing an MMP2-sensitive PEG-drug conjugate and cell-penetrating moiety, *Proc Natl Acad Sci U S A*, 2013, 110, 17047-17052.
24 K.N. Sugahara, T. Teesalu, P.P. Karmali, V.R. Kotamraju, L. Agemy, D.R. Greenwald and E. Ruoslahti, Coadministration of a tumor-penetrating peptide enhances the efficacy of cancer drugs, *Science*, 2010, 328, 1031-1035.
25 H. Maeda, G.Y. Bharate and J. Daruwalla, Polymeric drugs for efficient tumor-targeted drug delivery based on EPR-effect, *Eur J Pharm Biopharm*, 2009, 71, 409-419.
26 S. Tabaries, Z. Dong, M.G. Annis, A. Omeroglu, F. Pepin, V. Ouellet, C. Russo, M. Hassanain, P. Metrakos, Z. Diaz, M. Basik, N. Bertos, M. Park, C. Guettier, R. Adam, M. Hallett and P.M. Siegel, Claudin-2 is selectively enriched in and promotes the formation of breast cancer liver metastases through engagement of integrin complexes, *Oncogene*, 2011, 30, 1318-1328.
27 Z. Popovic, W. Liu, V.P. Chauhan, J. Lee, C. Wong, A.B. Greytak, N. Insin, D.G. Nocera, D. Fukumura, R.K. Jain and M.G. Bawendi, A nanoparticle size series for in vivo fluorescence imaging, *Angew Chem Int Ed Engl*, 2010, 49, 8649-8652.
28 R.K. Jain, Normalization of tumor vasculature: an emerging concept in antiangiogenic therapy, *Science*, 2005, 307, 58-62.
29 N. Bertrand, J. Wu, X. Xu, N. Kamaly and O.C. Farokhzad, Cancer nanotechnology: the impact of passive and active targeting in the era of modern cancer biology, *Adv Drug Deliv Rev*, 2014, 66, 2-25.
30 L. Zhu, P. Kate and V.P. Torchilin, Matrix metalloprotease 2-responsive multifunctional liposomal nanocarrier for enhanced tumor targeting, *ACS Nano*, 2012, 6, 3491-3498.
31 R. Roy, J. Yang and M.A. Moses, Matrix Metalloproteinases As Novel Biomarkers and Potential Therapeutic Targets in Human Cancer, *J Clin Oncol*, 2009, 27, 5287-5297.
32 L.L. Li, J.H. Xu, G.B. Qi, X. Zhao, F. Yu and H. Wang, Core-shell supramolecular gelatin nanoparticles for adaptive and "on-demand" antibiotic delivery, *ACS Nano*, 2014, 8, 4975-4983.
33 K. Shao, S. Singha, X. Clemente-Casares, S. Tsai, Y. Yang and P. Santamaria, Nanoparticle-Based Immunotherapy for Cancer, *Acs Nano*, 2015, 9, 16-30.
34 S. Ruan, M. Yuan, L. Zhang, G. Hu, J. Chen, X. Cun, Q. Zhang, Y. Yang, Q. He and H. Gao, Tumor microenvironment sensitive doxorubicin delivery and release to glioma using angiopep-2 decorated gold nanoparticles, *Biomaterials*, 2015, 37, 425-435.
35 E.A. Sykes, J. Chen, G. Zheng and W.C. Chan, Investigating the impact of nanoparticle size on active and passive tumor targeting efficiency, *ACS Nano*, 2014, 8, 5696-5706.
36 J.J. Liang, Y.Y. Zhou, J. Wu and Y. Ding, Gold nanoparticle-based drug delivery platform for antineoplastic chemotherapy, *Curr Drug Metab*, 2014, 15, 620-631.
37 C.C. Lee, A.T. Cramer, F.C. Szoka and J.M.J. Frechet, An intramolecular cyclization reaction is responsible for the in vivo inefficacy and apparent pH

insensitive hydrolysis kinetics of hydrazone carboxylate derivatives of doxorubicin, *Bioconjugate Chem*, 2006, 17, 1364-1368.
38 M. Niu, Y.W. Naguib, A.M. Aldayel, Y.C. Shi, S.D. Hursting, M.A. Hersh and Z. Cui, Biodistribution and in vivo activities of tumor-associated macrophage-targeting nanoparticles incorporated with doxorubicin, *Mol Pharm*, 2014, 11, 4425-4436.
39 Y. Xiao, H. Hong, V.Z. Matson, A. Javadi, W. Xu, Y. Yang, Y. Zhang, J.W. Engle, R.J. Nickles, W. Cai, D.A. Steeber and S. Gong, Gold Nanorods Conjugated with Doxorubicin and cRGD for Combined Anticancer Drug Delivery and PET Imaging, *Theranostics*, 2012, 2, 757-768.
40 F. Wang, Y. Wang, S. Dou, M. Xiong, T. Sun and J. Wang, Doxorubicin-tethered responsive gold nanoparticles facilitate intracellular drug delivery for overcoming multidrug resistance in cancer cells, *ACS Nano*, 2011, 5, 3679-3692.
41 S. Aryal, J.J. Grailer, S. Pilla, D.A. Steeber and S.Q. Gong, Doxorubicin conjugated gold nanoparticles as water-soluble and pH-responsive anticancer drug nanocarriers, *J Mater Chem*, 2009, 19, 7879-7884.
42 S. Ruan, X. Cao, X. Cun, G. Hu, Y. Zhou, Y. Zhang, L. Lu, Q. He and H. Gao, Matrix metalloproteinase-sensitive size-shrinkable nanoparticles for deep tumor penetration and pH triggered doxorubicin release, *Biomaterials*, 2015, 60, 100-110.
43 S. Ruan, Q. He and H. Gao, Matrix metalloproteinase triggered size-shrinkable gelatin-gold fabricated nanoparticles for tumor microenvironment sensitive penetration and diagnosis of glioma, *Nanoscale*, 2015, 7, 9487-9496.
44 P.M. Peiris, R. Toy, E. Doolittle, J. Pansky, A. Abramowski, M. Tam, P. Vicente, E. Tran, E. Hayden, A. Camann, A. Mayer, B.O. Erokwu, Z. Berman, D. Wilson, H. Baskaran, C.A. Flask, R.A. Keri and E. Karathanasis, Imaging Metastasis Using an Integrin-Targeting Chain-Shaped Nanoparticle, *ACS Nano*, 2012, 6, 8783-8795.
45 S. Ruan, J. Qian, S. Shen, J. Chen, J. Zhu, X. Jiang, Q. He, W. Yang and H. Gao, Fluorescent Carbonaceous Nanodots for Noninvasive Glioma Imaging after Angiopep-2 Decoration, *Bioconjug Chem*, 2014,
46 H. Lee, M.Y. Lee, S.H. Bhang, B.S. Kim, Y.S. Kim, J.H. Ju, K.S. Kim and S.K. Hahn, Hyaluronate-Gold Nanoparticle/Tocilizumab Complex for the Treatment of Rheumatoid Arthritis, *Acs Nano*, 2014, 8, 4790-4798.
47 C.H. Liang, W.L. Ye, C.L. Zhu, R. Na, Y. Cheng, H. Cui, D.Z. Liu, Z.F. Yang and S.Y. Zhou, Synthesis of doxorubicin alpha-linolenic acid conjugate and evaluation of its antitumor activity, *Mol Pharm*, 2014, 11, 1378-1390.
48 N.V. Rao, M.N. Ganivada, S. Sarkar, H. Dinda, K. Chatterjee, T. Dalui, J. Das Sarma and R. Shunmugam, Magnetic Norbornene Polymer as Multiresponsive Nanocarrier for Site Specific Cancer Therapy, *Bioconjugate Chem*, 2014, 25, 276-285.
49 H. Gao, Z. Yang, S. Zhang, S. Cao, S. Shen, Z. Pang and X. Jiang, Ligand modified nanoparticles increases cell uptake, alters endocytosis and elevates glioma distribution and internalization (vol 3, 2534, 2013), *Scientific Reports*, 2014, 4,
50 H. Gao, Z. Yang, S. Zhang, Z. Pang, Q. Liu and X. Jiang, Study and evaluation of mechanisms of dual targeting drug delivery system with tumor microenvironment assays compared with normal assays, *Acta Biomater*, 2014, 10, 858-867.
51 S.M. Sagnella, H. Duong, A. MacMillan, C. Boyer, R. Whan, J.A. McCarroll, T.P. Davis and M. Kavallaris, Dextran-Based Doxorubicin Nanocarriers with Improved Tumor Penetration, *Biomacromolecules*, 2014, 15, 262-275.
52 K.Y. Huang, H.L. Ma, J. Liu, S.D. Huo, A. Kumar, T. Wei, X. Zhang, S.B. Jin, Y.L. Gan, P.C. Wang, S.T. He, X.N. Zhang and X.J. Liang, Size-Dependent Localization and Penetration of Ultrasmall Gold Nanoparticles in Cancer Cells, Multicellular Spheroids, and Tumors in Vivo, *Acs Nano*, 2012, 6, 4483-4493.
53 H. Gao, Z. Yang, S. Zhang, S. Cao, Z. Pang, X. Yang and X. Jiang, Glioma-homing peptide with a cell-penetrating effect for targeting delivery with enhanced glioma localization, penetration and suppression of glioma growth, *J Controlled Release*, 2013, 172, 921-928.

54 H. Gao, Y. Xiong, S. Zhang, Z. Yang, S. Cao and X. Jiang, RGD and Interleukin-13 Peptide Functionalized Nanoparticles for Enhanced Glioblastoma Cells and Neovasculature Dual Targeting Delivery and Elevated Tumor Penetration, *Molecular Pharmaceutics*, 2014, 11, 1042-1052.
55 Y. Liu, M. Ji, M.K. Wong, K.I. Joo and P. Wang, Enhanced Therapeutic Efficacy of iRGD-Conjugated Crosslinked Multilayer Liposomes for Drug Delivery, *Biomed Research International*, 2013,
56 T. Stylianopoulos, C. Wong, M.G. Bawendi, R.K. Jain and D. Fukumura, Multistage Nanoparticles for Improved Delivery into Tumor Tissue, *Nanomedicine: Cancer, Diabetes, and Cardiovascular, Central Nervous System, Pulmonary and Inflammatory Diseases*, 2012, 508, 109-130.
57 J.W. Baish, Y. Gazit, D.A. Berk, M. Nozue, L.T. Baxter and R.K. Jain, Role of tumor vascular architecture in nutrient and drug delivery: an invasion percolation-based network model, *Microvasc Res*, 1996, 51, 327-346.
58 H. Cabral, Y. Matsumoto, K. Mizuno, Q. Chen, M. Murakami, M. Kimura, Y. Terada, M.R. Kano, K. Miyazono, M. Uesaka, N. Nishiyama and K. Kataoka, Accumulation of sub-100 nm polymeric micelles in poorly permeable tumours depends on size, *Nat Nanotechnol*, 2011, 6, 815-823.
59 H. Gao, Z. Yang, S. Cao, Y. Xiong, S. Zhang, Z. Pang and X. Jiang, Tumor cells and neovasculature dual targeting delivery for glioblastoma treatment, *Biomaterials*, 2014, 35, 2374-2382.
60 S.D. Perrault, C. Walkey, T. Jennings, H.C. Fischer and W.C.W. Chan, Mediating Tumor Targeting Efficiency of Nanoparticles Through Design, *Nano Lett*, 2009, 9, 1909-1915.
61 J.S. Nam, M. Terabe, M. Mamura, M.J. Kang, H. Chae, C. Stuelten, E. Kohn, B. Tang, H. Sabzevari, M.R. Anver, S. Lawrence, D. Danielpour, S. Lonning, J.A. Berzofsky and L.M. Wakefield, An anti-transforming growth factor beta antibody suppresses metastasis via cooperative effects on multiple cell compartments, *Cancer Res*, 2008, 68, 3835-3843.

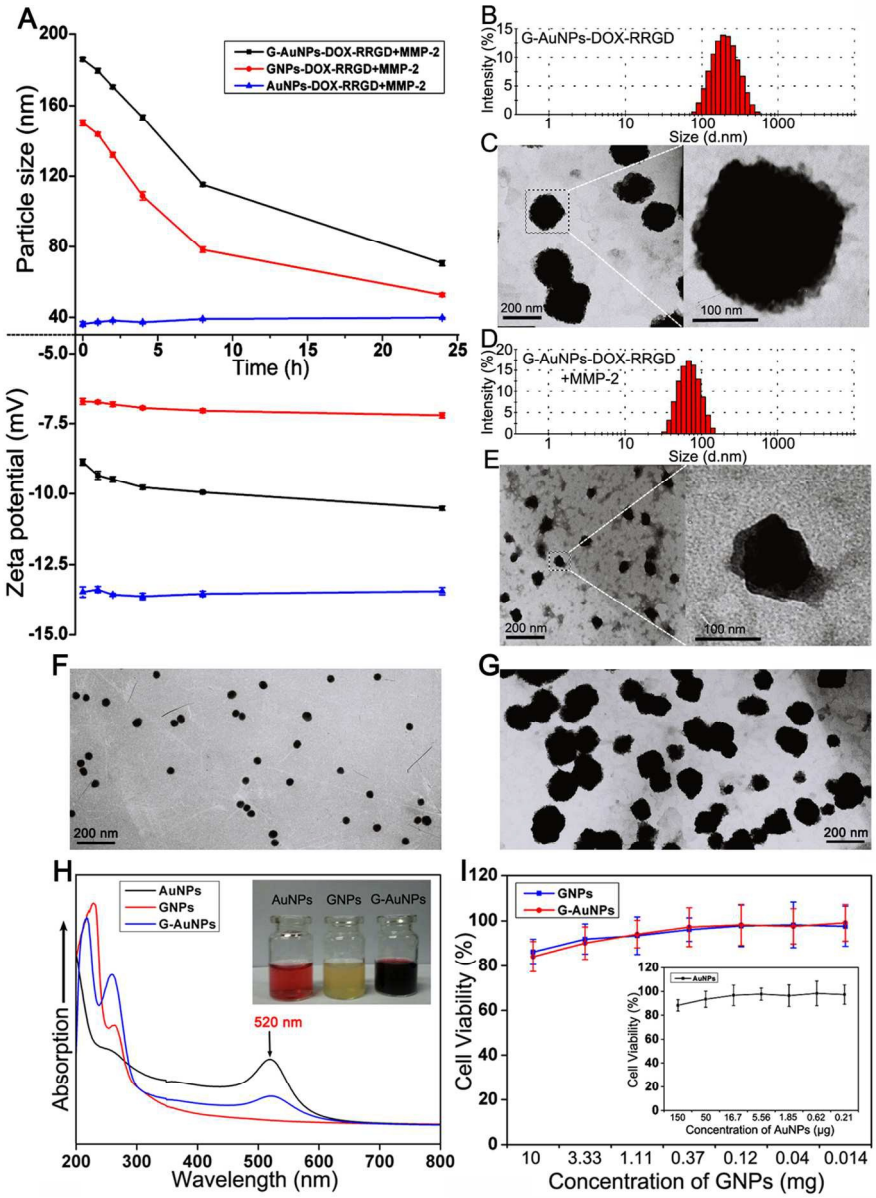

110x149mm (300 x 300 DPI)

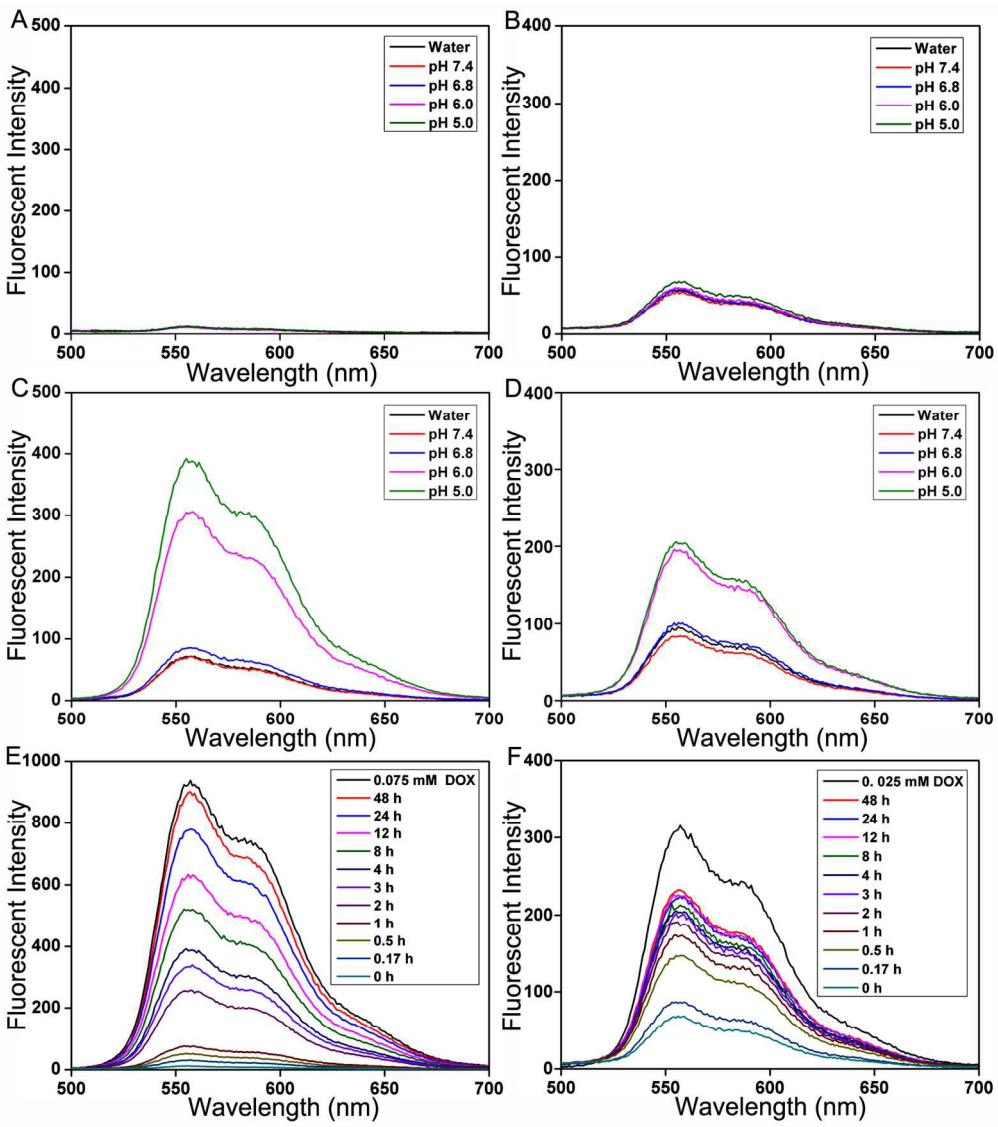

140x158mm (300 x 300 DPI)

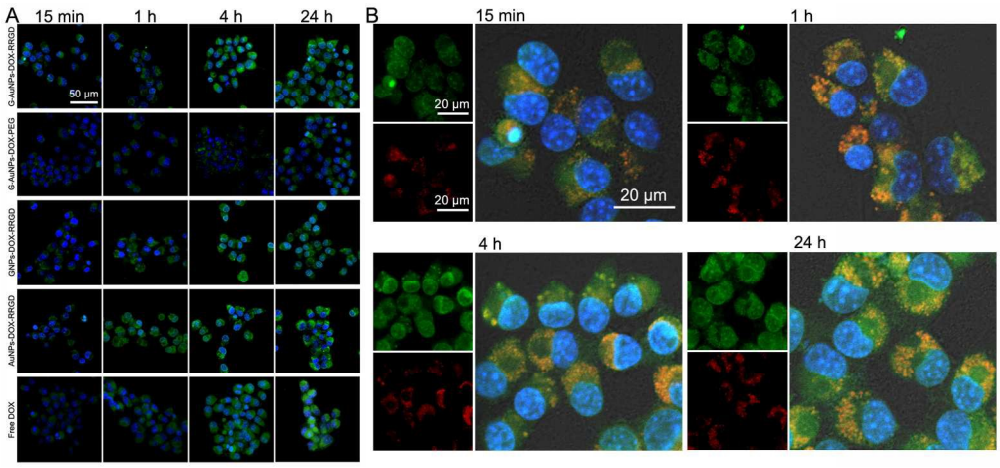

169x78mm (300 x 300 DPI)

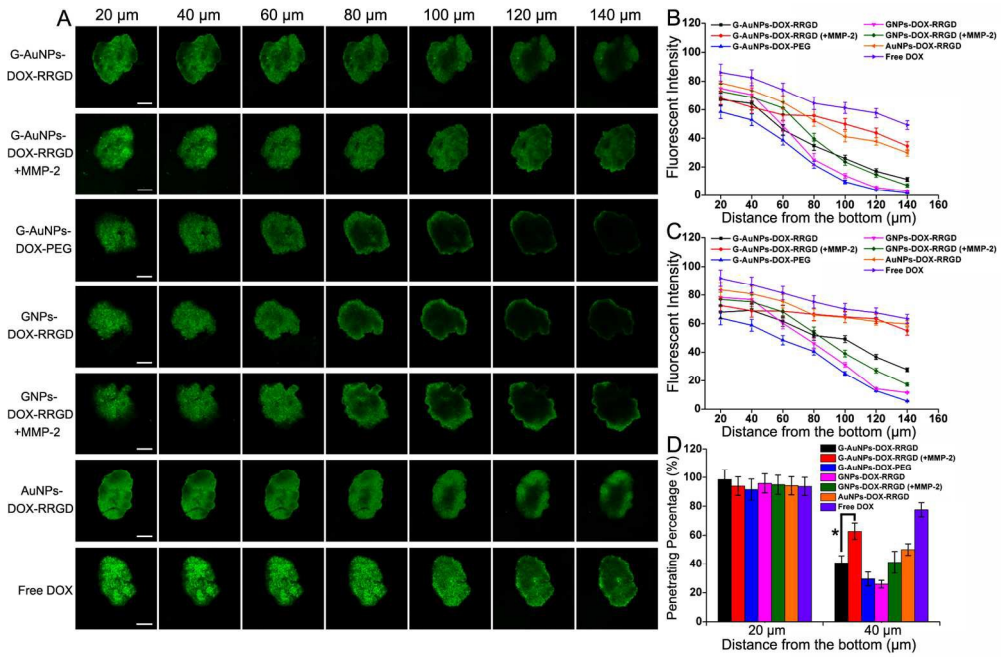

159x104mm (300 x 300 DPI)

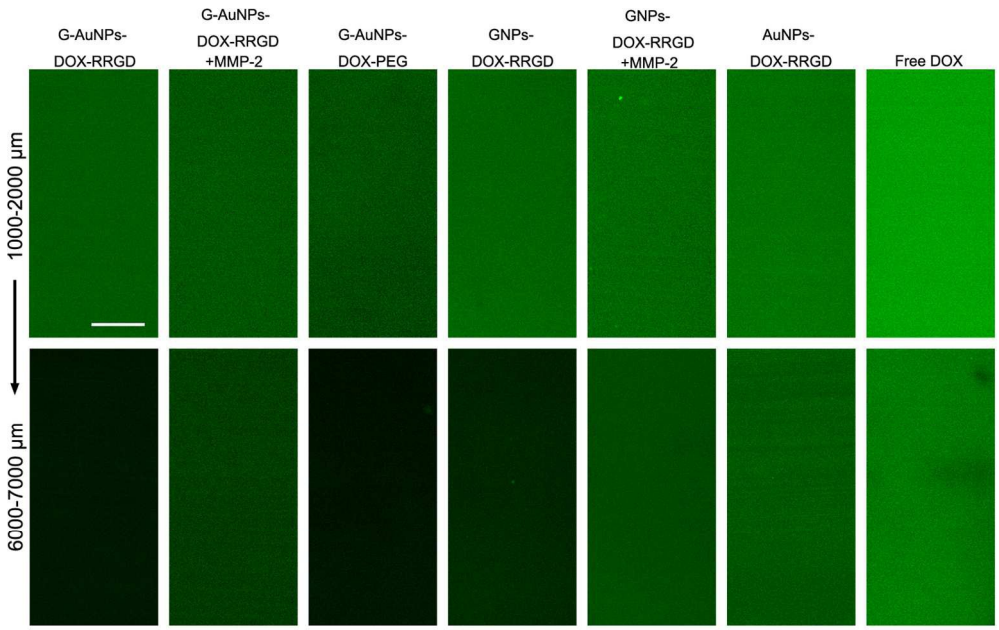

140x88mm (300 x 300 DPI)

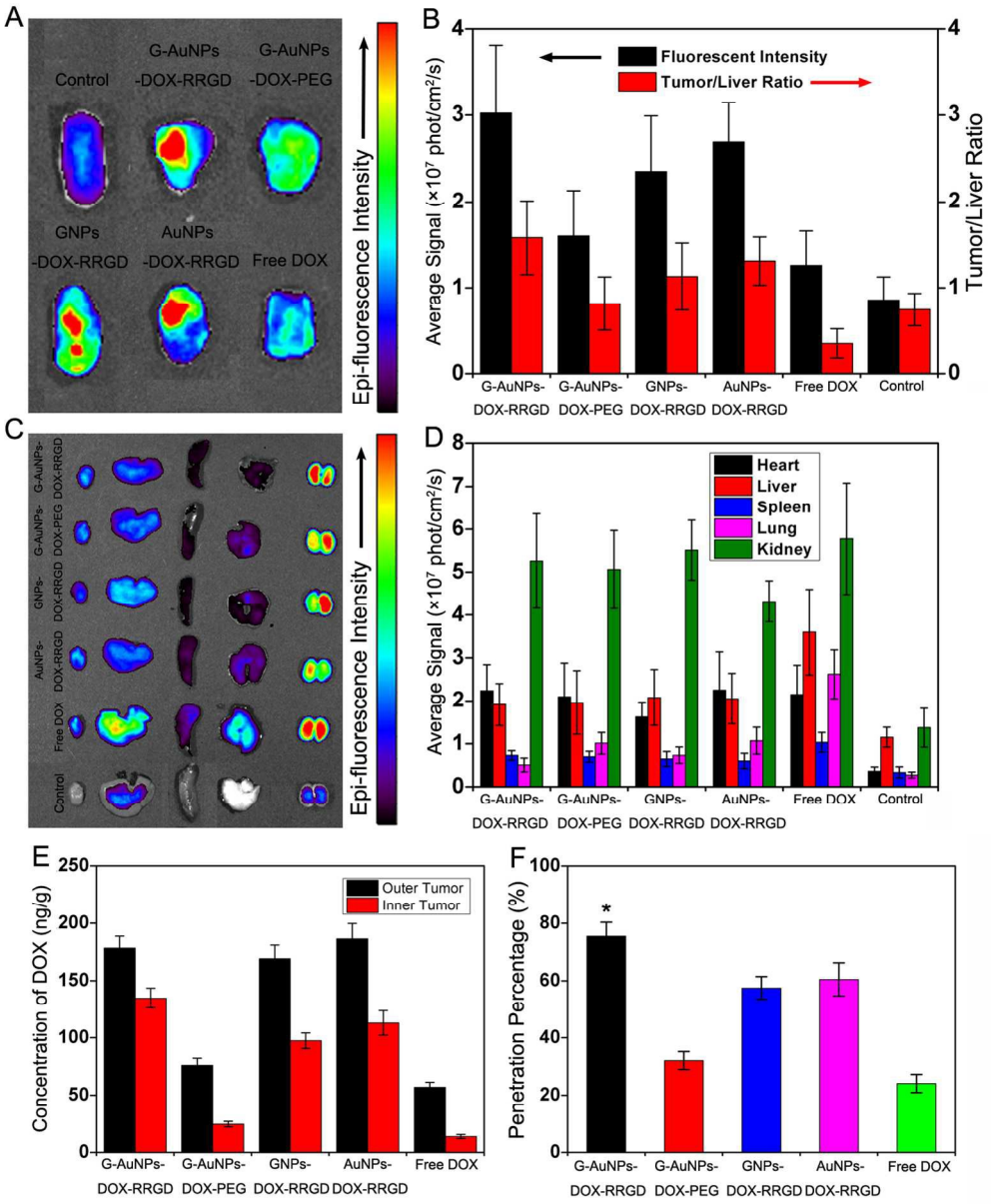

125x151mm (300 x 300 DPI)

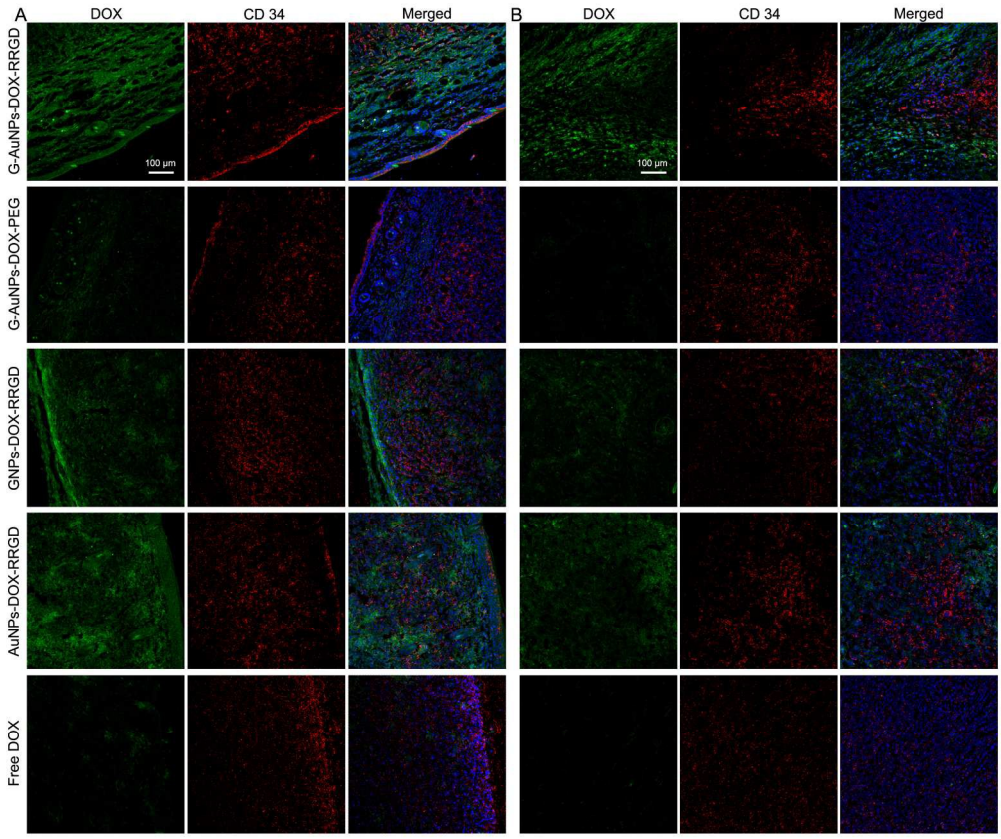

192x160mm (300 x 300 DPI)

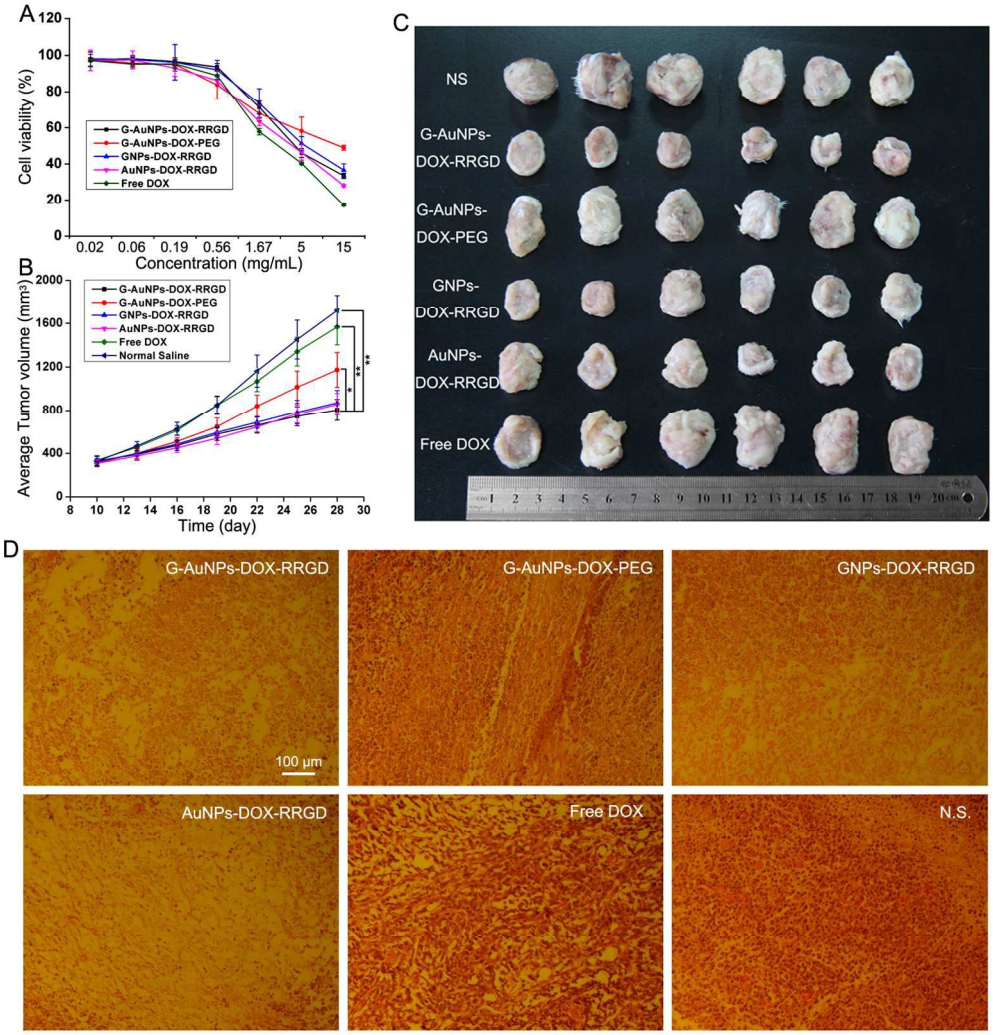

151x158mm (300 x 300 DPI)

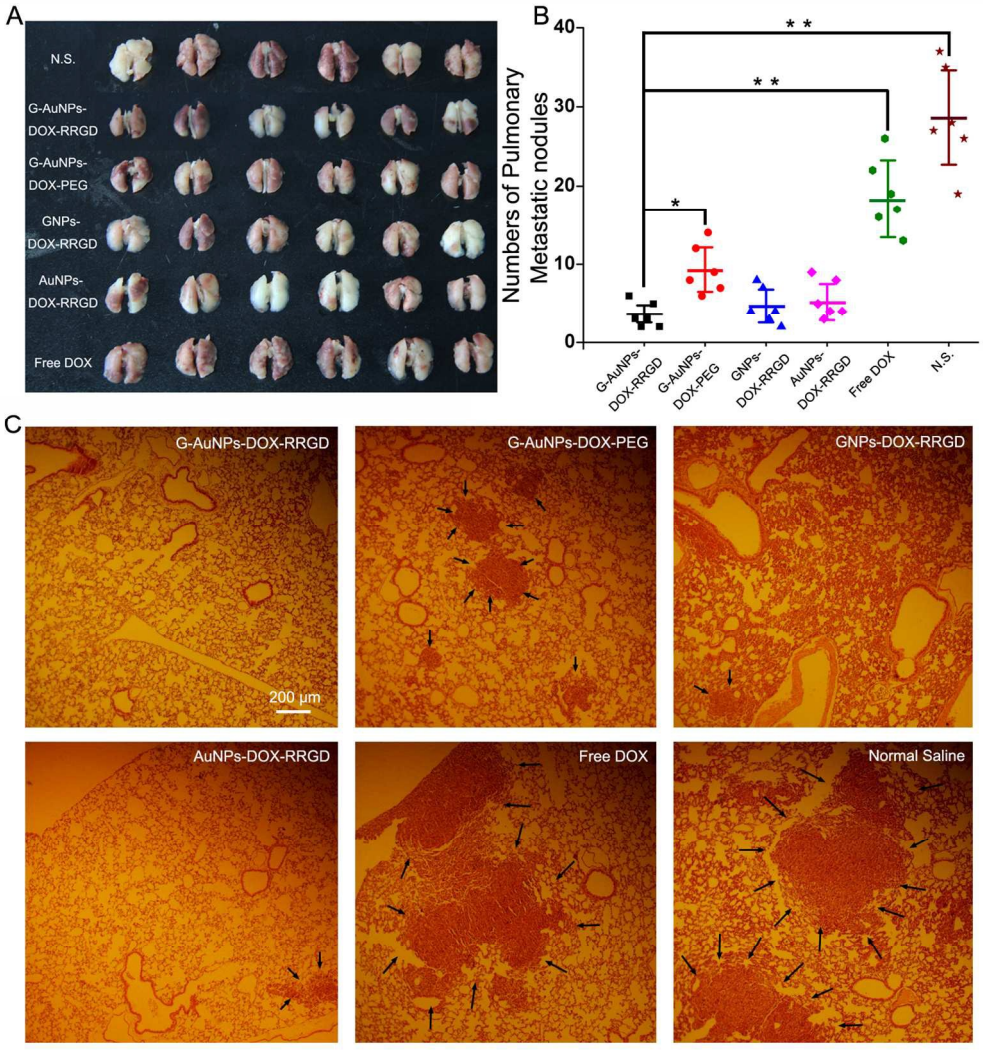

138x145mm (300 x 300 DPI)

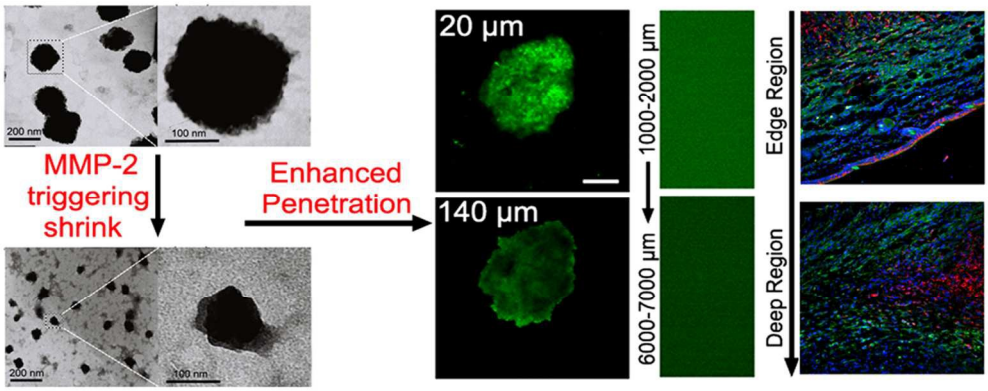

105x42mm (300 x 300 DPI)